

# Acknowledgement

First of all, I would like to thank my supervisor, Associate Professor Goki Eda, for allowing me to take on this Final Year Project in Eda Lab. His guidance and advice throughout this one year duration was helpful in pushing me towards the right direction. Despite my reluctance to ask questions, he is always willing to answer my queries and correct any misconception that I may have.

I would also like to extend my heartfelt thanks to Chen Ming Jun, my mentor, for being there for me all the way. Despite being busy with his own research and classes, he is always accommodating and has assisted me whenever I was having trouble with any aspect of the project, such as operating the equipment or even explaining in-depth portions of the theory which I did not understand. Not only that, but he has thought me everything I needed to know on how to prepare my first device and conduct the experimental measurements on them. I am extremely grateful for all the help he has extended towards me. This thesis would not have been possible without his involvement.

Additionally, a special thanks to all the people at Eda Lab who assisted me throughout the project, especially to Justin, who wrote the code for the photocurrent mapping software and having taught me initially the few basics techniques of device fabrication, as well as Dr. Neo for his SHG mapping setup and clarifying any doubts that I had along the way.

Last but not least, I would like to thank my friends, family and loved ones for being there and cheering for me through my final year. It was a challenging project but their presence had made the time much more enjoyable.

# Abstract

The bulk photovoltaic effect (BPVE) is the process in which a steady photocurrent is produced within a homogeneous material lacking centrosymmetric properties without the need of an initially applied potential difference. In this paper, we examine the BPVE in the non-centro symmetric 2D material Palladium Selenide, or  $\text{PdSe}_2$ . As broken inversion symmetry is a prerequisite for shift current and only even layers of  $\text{PdSe}_2$  have broken inversion symmetry, we therefore expect shift current to be present in such even-layers when an external electric field, such as light, is applied to it. Second Harmonic Generation (SHG) and photocurrent mapping were performed using an in-house laser set-up. The prerequisite of non-centrosymmetry for SHG response in  $\text{PdSe}_2$  was experimentally obtained and verified through the SHG mapping. Photocurrent characteristics of  $\text{PdSe}_2$  was measured but its power dependence was unable to be verified confidently due to the unexpected flipping of photocurrent direction at large power. Lastly, a photocurrent mapping of the shift current was obtained for electrode 1,4 in Flake 2, but it was inconclusive as such result was unobtainable on further mapping. Additionally, the heating of the sample and Schottky barrier were of large enough magnitude to dominate the shift current.

# Contents

<b>1</b>	<b>Introduction</b>	<b>5</b>
1.1	2D Materials . . . . .	5
1.2	Shift Current . . . . .	7
1.3	Second-Harmonic Generation . . . . .	7
1.4	Schottky Barrier Effect . . . . .	9
1.5	Ultrasonic Water Bath . . . . .	11
1.6	Atomic Force Microscopy . . . . .	11
1.7	SHG Mapping . . . . .	11
1.8	Spin Coating and Laser Lithography . . . . .	14
1.9	Physical Vapor Deposition (PVD) System . . . . .	14
1.10	Photocurrent Measurement . . . . .	15
<b>2</b>	<b>Methodology</b>	<b>18</b>
2.1	Sample Fabrication . . . . .	18
2.2	Atomic Force Microscopy Process . . . . .	19
2.3	Laser Lithography Process . . . . .	20
2.4	Vapor Deposition Process . . . . .	21
2.5	I/V Sweep . . . . .	22
2.6	Photocurrent measurement . . . . .	22
<b>3</b>	<b>Results &amp; Discussion</b>	<b>24</b>
3.1	Flakes from mechanical exfoliation . . . . .	24
3.2	Atomic Force Microscopy Measurement . . . . .	25
3.3	SHG Mapping . . . . .	28
3.4	I/V Sweep . . . . .	31
3.5	Photocurrent Measurement . . . . .	32
3.6	Photocurrent Mapping . . . . .	34
<b>4</b>	<b>Conclusion</b>	<b>36</b>
4.1	Summary . . . . .	36
4.2	Follow-up to Experiments . . . . .	36
4.3	Future Research . . . . .	36

<b>5</b>	<b>Appendix</b>	<b>38</b>
5.1	Electrode Design . . . . .	38
5.2	Unused Samples . . . . .	39
<b>6</b>	<b>References</b>	<b>41</b>

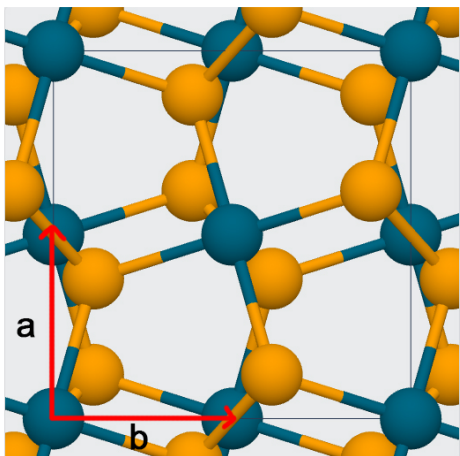
# 1 Introduction

## 1.1 2D Materials

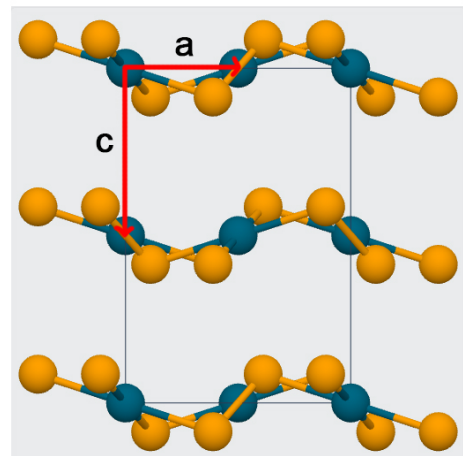
When graphene was first identified in 2004, it caught a lot of interest due to its high electron mobility and Young's Modulus alongside its optical transparency, to name a few of its properties. Ever since then, research into other materials that may possess such properties have greatly expanded to include phosphorenes, borophenes, MXenes and transition-metal dichalcogenides (TMDCs).

In short, two-dimensional (2D) materials may be defined as one to ten atom thick isolated layers that may persist without the help of a substrate<sup>1</sup>. Considering their large carrier mobility and electrical properties that may vary with crystal orientation, 2D materials are good candidates for electrical devices such as transistors, photodetectors and photovoltaic cells<sup>2</sup>. One such 2D material is PdSe<sub>2</sub>, which has garnered attention due to its unique pentagonal structure that differs from most hexagonal 2D materials that are highly symmetric.

In a unit cell of PdSe<sub>2</sub>, there consists four Pd atoms and eight Se atoms. Each Pd atoms are bonded to four other Se atoms while two adjacent Se atoms will be covalently bonded to one another. Compared to Mo and W, Pd has a nearly filled d-shell, resulting in stronger hybridization with p-shells from chalcogenides like Se, and therefore, stronger covalent bonds. The layers of PdSe<sub>2</sub> are then held together by Van der Waals forces. These gives rise to its puckered-pentagonal layered structure. Its lattice parameters, *a*, *b* and *c* are 5.75, 5.85 and 7.69Å respectively. PdSe<sub>2</sub> also has a pucker height of 1.6Å. It also has a tunable bandgap ranging from 1.6eV for monolayers to 0.25 in the bulk<sup>3</sup>. Due to the asymmetry found in even-layered PdSe<sub>2</sub>, they are therefore expected to also show non-linear optical properties, such as second-harmonic generation. Even-layered PdSe<sub>2</sub> has an orthorhombic Bravais lattice, is birefringent and belongs to the Pca2<sub>1</sub> space group<sup>3</sup>.



(a)



(b)

**Figure 1:** Dark blue represents Pd atoms and yellow represents Se atoms. (a) Top profile of unit cell of PdSe<sub>2</sub>. (b) Side profile of unit cell of PdSe<sub>2</sub>.

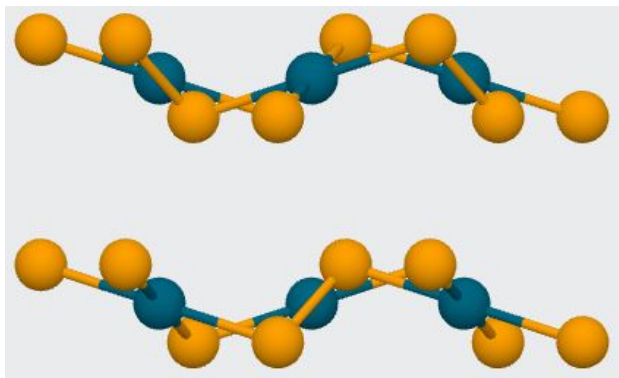


**Figure 2:** Bilayer PdSe<sub>2</sub>, where the plane of symmetry is between the two layers, showing broken inversion symmetry.

## 1.2 Shift Current

Earlier mentioned, BPVE is the process in which a steady photocurrent is produced within a homogeneous material lacking centrosymmetric properties without the need of an initially applied potential difference. As the shift current is one of the main proponents of BPVE<sup>4</sup>, we therefore examine the behavior of BPVE in PdSe<sub>2</sub> through the shift current. For shift current, charge carriers when excited by light, undergo coherent excitation. In an n-level energy system, electrons from the ground state can be excited to a higher energy n-level state by photons with frequencies  $\omega$  or  $-\omega$ . If these excitation amplitudes interfere asymmetrically, there would then be direct current. In general, the shift current can be explained by the equation:

$$J_q = \sigma_{rsq} E_r E_s \quad (1)$$

where  $J_q$  is the shift current,  $\sigma_{rsq}$  is current density generated per incident intensity, also known as the material-dependant response function, and  $E_r, E_s$  are the external electric field applied. For a material with inversion symmetry, under inversion operation,  $J_q$  and the product of  $E_r E_s$  each pick up a negative sign while  $\sigma_{rsq}$  remains unchanged. This therefore explains why there could only be shift current in a system with broken inversion symmetry.

## 1.3 Second-Harmonic Generation

Generally, a nonlinear optical process obeys the equation:

$$\mathbf{P}(t) = \epsilon_0 (E_S^{(1)} \mathbf{E}(t) + E_S^{(2)} \mathbf{E}^2(t) + E_S^{(3)} \mathbf{E}^3(t) + \dots) \quad (2)$$

where the second order would be:

$$E(2\omega) \propto \mathbf{P}^{(2)}(2\omega) = E_S^{(2)} \mathbf{E}(\omega) \mathbf{E}(\omega) \quad (3)$$

Electric susceptibility, or  $E_S$  in the equation above, is a dimensionless proportionality that indicates the extent of polarization of a dielectric material in the presence of an external electric field.

Second-Harmonic Generation (SHG), or frequency doubling is one of the second-order non-linear optical process that occur only in non-centrosymmetric materials. It occurs when two electrons with frequency  $\omega$  interacts in the optical medium and produce a photon with frequency  $2\omega$  under conservation law of energy.

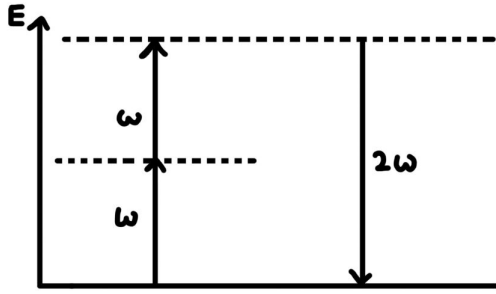


**Figure 3:** Energy level diagram for SHG process, where an incoming photon produces an outgoing photon with a doubled frequency.

As SHG is affected by the polarization angle of the incoming light with respect to the crystallographic orientation of a material, we can then use an SHG mapping to determine the crystal axis of a sample<sup>5</sup>. This can be seen when we let:

$$d_{ijk} = \frac{1}{2} E_{S_{ijk}}^2 \quad (4)$$

Consider now the Kleinman symmetry condition. When the applied frequency is much smaller than the lowest resonance frequency of the material, the non-linear susceptibility essentially becomes a constant independent of the frequency. Additionally, the medium may be considered lossless and full permutation symmetry is considered valid<sup>6</sup>. Therefore, the last two indices of  $d_{ijk}$  is permutable. By introducing  $d_{il}$ , where:

$$\begin{aligned} jk : & \quad 11 \quad 22 \quad 33 \quad 23, 32 \quad 31, 13 \quad 12, 21 \\ l : & \quad 1 \quad 2 \quad 3 \quad 4 \quad 5 \quad 6 \end{aligned}$$

Eqn.3 can then be written as:

$$P_i(\omega_n + \omega_m) = \epsilon_0 \sum_{jk} \sum_{nm} 2d_{ijk} E_j(\omega_n) E_k(\omega_m) \quad (5)$$

If Eqn.5 is expressed as a matrix, then  $d_{il}$  can be written as:

$$d_{il} = \begin{bmatrix} d_{11} & d_{12} & d_{13} & d_{14} & d_{15} & d_{16} \\ d_{21} & d_{22} & d_{23} & d_{24} & d_{25} & d_{26} \\ d_{31} & d_{32} & d_{33} & d_{34} & d_{35} & d_{36} \end{bmatrix} \quad (6)$$

where using the Kleinman symmetry would turn it to:

$$d_{il} = \begin{bmatrix} d_{11} & d_{12} & d_{13} & d_{14} & d_{15} & d_{16} \\ d_{16} & d_{22} & d_{23} & d_{24} & d_{14} & d_{12} \\ d_{15} & d_{24} & d_{33} & d_{23} & d_{13} & d_{14} \end{bmatrix} \quad (7)$$

& thus:

$$\begin{bmatrix} P_x(2\omega) \\ P_y(2\omega) \\ P_z(2\omega) \end{bmatrix} = 4\epsilon_0 \begin{bmatrix} d_{11} & d_{12} & d_{13} & d_{14} & d_{15} & d_{16} \\ d_{16} & d_{22} & d_{23} & d_{24} & d_{14} & d_{12} \\ d_{15} & d_{24} & d_{33} & d_{23} & d_{13} & d_{14} \end{bmatrix} \begin{bmatrix} E_x(\omega_1)E_x(\omega_2) \\ E_y(\omega_1)E_y(\omega_2) \\ E_z(\omega_1)E_z(\omega_2) \\ E_y(\omega_1)E_z(\omega_2) + E_z(\omega_1)E_y(\omega_y) \\ E_x(\omega_1)E_z(\omega_2) + E_z(\omega_1)E_x(\omega_y) \\ E_x(\omega_1)E_y(\omega_2) + E_y(\omega_1)E_x(\omega_y) \end{bmatrix} \quad (8)$$

where depending on the space group and spatial symmetry, some of the factors of  $d_{il}$  will turn to 0 and gain polarization dependence factors  $\theta$ , the angle between the propagation vector and crystalline z axis (optical axis) and  $\phi$ , the angle between the propagation vector and crystalline xz plane, which can be obtained from *Non-Linear Optics* by Robert W. Boyd, Section 2.11. For PdSe<sub>2</sub>, the relationship between the SHG intensity and its crystal axis is related as<sup>7</sup>:

$$I \propto [d_{11}\cos\theta^3 + (d_{21} + 2d_{16})\cos\theta^2\sin\theta + (d_{12} + 2d_{26})\cos\theta^2 + d_{22}\sin\theta^3]^2 \quad (9)$$

#### 1.4 Schottky Barrier Effect

At the border between the metal electrode and semiconductor sample, there will be a potential barrier known as the *Schottky Barrier*. Generally, this occurs when the work function of the metal used for the electrode is less than that of work function of the semiconductor sample for an n-type semiconductor. Similarly, for p-type semiconductors, it has to be that the work function of the electrode be higher than that of the semiconductor.

The work function of the metal is defined to be the difference between its vacuum energy, the energy needed for an electron to escape from the surface of the metal into vacuum, and its Fermi Energy, the energy difference between the highest and lowest single-occupied state at absolute zero, as described by the following equation:

$$W = E_0 - E_F \quad (10)$$

where  $E_0$  is the vacuum energy while  $E_F$  is the Fermi Energy.

Similarly, the work function of the semiconductor would be defined as the difference between the vacuum energy and the conduction band energy level,  $E_C$ . This difference is known as the electron affinity,  $\chi$ , which is an intrinsic property of the semiconductor. However, if there is doping, then the factor of the difference between the conduction band energy level and the Fermi Energy level has to be included also, giving rise to the equation:

$$W = \chi + (E_C - E_F) \quad (11)$$

When these materials are then brought together, there will be a 'bending' of the Fermi energy level as the Fermi energy level of the metal and semiconductor equalizes due to the movement of charges between them, resulting in the formation of an energy barrier. For electrons, the barrier height,  $\phi_e$ , is defined as the difference between the metal work function and  $\chi$  of the semiconductor. Similarly, the barrier height for holes,  $\phi_h$ , would then be the difference between the energy gap of the semiconductor and  $\chi_e$ .

If this barrier height is large enough, a depletion zone would form near the junction between the semiconductor and metal. For an n-type semiconductor, when a forward voltage bias is applied, electrons from the semiconductor would be able to overcome the barrier height and transfer over to the metal, resulting in a current flow towards the metal. For a p-type semiconductor, the same principal applies, only vice-versa.

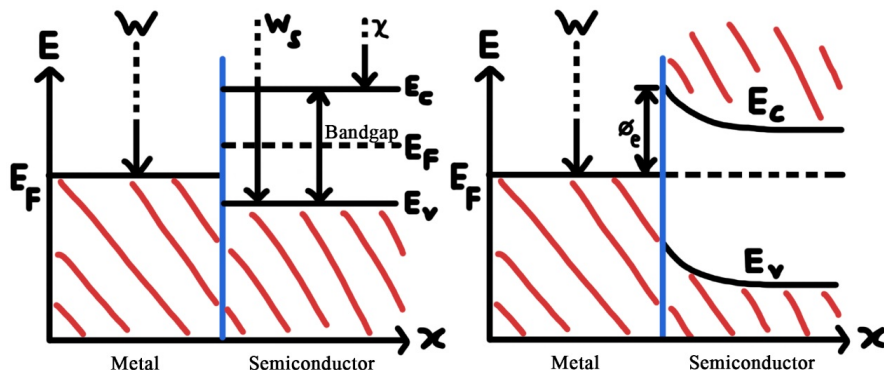


**Figure 4:** Energy level diagram between a metal and n-type semiconductor before contact (left) and after (right).

## 1.5 Ultrasonic Water Bath

An ultrasonic bath consists of the bath, the generator and transducer. The generator supplies the AC power needed by a piezoelectric crystal in the transducer. This crystal converts the electrical energy into ultrasonic energy through its changing shape and size due to the piezoelectric effect. A radiating plate within the transducer absorbs these ultrasonic energy and converts it to mechanical energy as fluid waves. Bubbles are then formed within the liquid which then implodes upon the sample surface, scrubbing it clean by dislodging any contaminants present.

## 1.6 Atomic Force Microscopy

An AFM consists of four components: a laser, a sample stage, a cantilever and a four quadrant photodetector. An AFM operates on the localized mechanical forces experienced by its cantilever. A cantilever with a very sharp tip is brought extremely close to the sample surface slowly. The attractive forces between the tip and the surface causes the cantilever to deflect towards the surface, therefore allowing the machine to detect the cantilever to be brought closer. However, if it is brought too close, then the cantilever deflected away from the surface and the machine pulls the tip back up. These deflection towards or away from the surface are deflected by a laser spot that is beamed onto the tip. The deflection of the cantilever causes a change in the direction of the beam and these variations in the light intensity are then measured by a photodiode. Thus, by scanning the cantilever over the surface of a flake, a detailed microscopic topography of the surface can be obtained.

## 1.7 SHG Mapping

Using the principles outlined in Section 2.3 regarding Second Harmonic Generation, a 2D map of the second-harmonic response from a sample can be obtained when it is exposed to laser. An in-house laser setup was used for the SHG mapping. It consists of: a piezoelectric stage to house the sample, a Glan-Taylor polarizer, a quarter waveplate, a Thorlabs AHWP10M-1600 achromatic half waveplate fixed on a motorized rotation mount to vary the polarization, two Thorlabs DML P950R long pass dichroic mirror, a powermeter, two Newport 10BC16NP.6 non-polarizing beamsplitter cube, a 950nm short pass filter (SPF), a pco4.2 camera, an Olympus LCPLN100x 0.85NA objective lens and a Thorlabs AC254-050-B-ML achromatic doublet.

A laser beam of desired wavelength first passes through the Glan-Taylor polarizer and becomes linearly polarized. It then enters the quarter waveplate so as to remove any circular polarization. Afterwards, the laser continues through a longpass dichroic mirror where wavelength of above 950nm is transmitted through while the rest is reflected off. Next, it enters the beamsplitter cube where half of the laser is reflected. This reflected laser enters into a powermeter so as to measure the power of the laser. However, this component is removable if such measurement is not required. The non-reflected portion then passes into an achromatic half waveplate where chromatic aberrations are removed. It then passes into another similar longpass dichroic mirror, into the objective lens and hits the sample on the piezo stage. SHG occurs and the post-SHG light produced from the sample now re-encounters the longpass dichroic mirror, but due to frequency doubling, its wavelength is now below the cut-off wavelength of 950nm and is instead reflected. It passes the 950SPF where wavelength above 950nm is not transmitted through. Those that do hit another beamsplitter cube again. Half of them is then reflected into a camera while the rest enters an achromatic doublet to reduce chromatic aberration before entering the spectrometer so that the necessary information needed regarding the SHG laser can be obtained.

By varying the voltage across the piezoelectric stage, the sample can be shifted in a controlled manner such that the laser can scan through a desired area, therefore producing the SHG mapping of the sample.

## setup

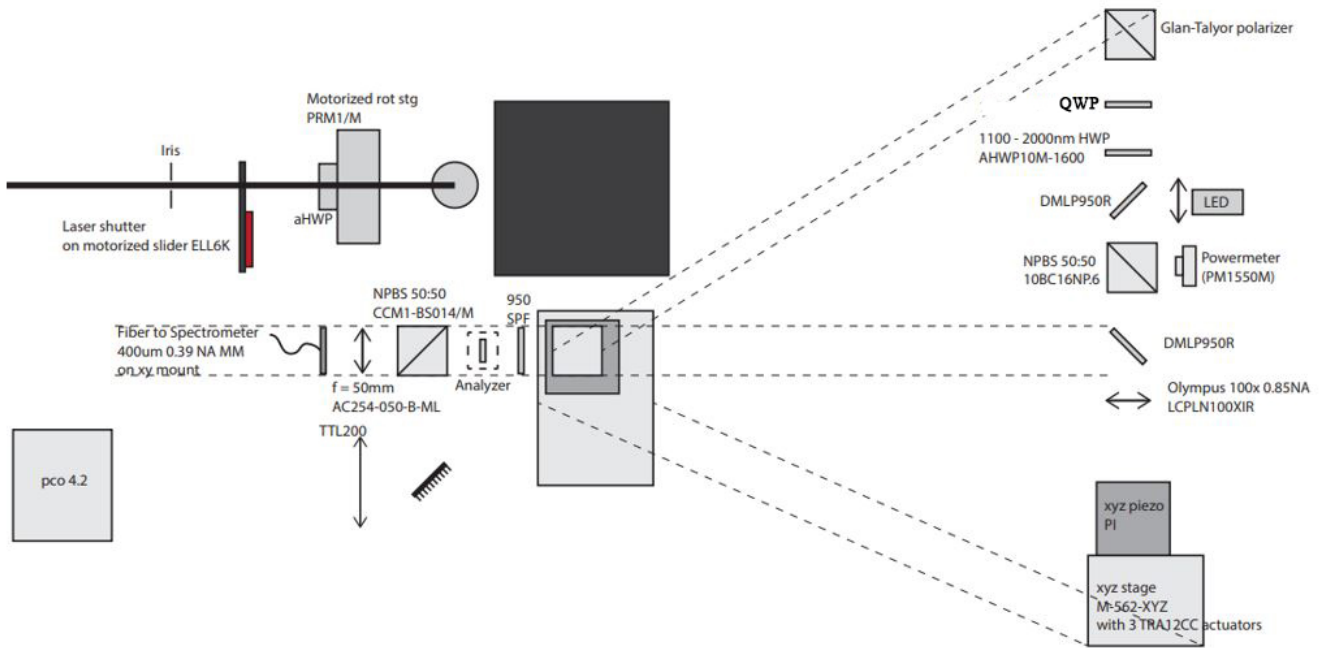


**Figure 5:** A labelled schematic of the in-house setup used to produce the SHG map.

## 1.8 Spin Coating and Laser Lithography

Spin coating is a technique used to produce films of generally uniform thickness through rapidly spinning the sample. Assuming that there is no evaporation effect taking place and that the viscosity of the fluid used will not be changed by stress, a non-volatile, viscous fluid on an infinite rotating disk would obey the equation:

$$h = \frac{h_0}{\sqrt{1 + \frac{4\rho\omega^2}{3\eta} h_0^2 t}} \quad (12)$$

where  $h$  is the final thickness of the fluid layer,  $h_0$  is the original uniform thickness of fluid layer before spinning at  $t = 0$ ,  $\rho$  is the density of the fluid,  $\omega$  is the angular velocity of the disk,  $\eta$  is the viscosity of the fluid and  $t$  is the duration of spinning.

After spin coating, the sample is soft-baked at a certain temperature, depending on the photoresist used. This soft-baking is to dehydrate the solvent within the photoresist and make them solidify.

The photoactive resins that are used are S1805 and LOR3A. S1805 contains photoactive compounds diazonaphthoquinones (DNQ) that becomes activated and soluble in photoresist developers when exposed to strong UV light at 390nm provided by the laser writer. Meanwhile, LOR3A contains polydimethylglutarimide (PMGI) which is insoluble in most photoactive resins, thus preventing intermixing with S1805. However, LOR3A is still soluble in photoresist developers. S1805 and LOR3A can both be removed using PG Remover.

## 1.9 Physical Vapor Deposition (PVD) System

In a PVD system, the process is generally done in an environment with pressure of about  $10^{-5}$  Torr, which is obtained through the evacuation of the chamber using a vacuum pump. This is as such so that the vaporized atoms of the material have a larger mean free path, minimizing unwanted collision that it may experience before reaching the target, therefore resulting in a purer coating.

Firstly, the material that is to be coated upon the target is heated up by direct current. The vaporized atoms then travel through the chamber and impinges onto the target sample where

it then condenses, growing a thin film over the sample.

For the region of pressure of about  $10^{-7}$  Torr, an ionization gauge is preferably used to monitor the pressure in the chamber. Within the system there is a filament that is heated so as to produce electrons, which are then attracted to a cathode. Due to its open-coiled grid structure, these electrons can overshoot the cathode and return, therefore increasing their lifetime and chance of colliding with a gas molecule. This collision produces positive ions which are then collected and the pressure of the chamber can be detected through the equation:

$$I^+ = SPI_e \quad (13)$$

where  $I^+$  is the ion current produced,  $I_e$  is the electron emission current from the filament,  $P$  is the pressure in the chamber and  $S$  is the gas ionization sensitivity factor.

A commonly used method to monitor the rate of deposition flux is through a quartz crystal oscillator monitor. A quartz crystal disc in between a pair of electrodes is placed within the path of the evaporation flux. An alternating current is then applied to it, causing it to oscillate at its natural frequency,  $f_0$ , due to piezoelectric effect. As the flux then condenses on the crystal, its mass changes and therefore, so does its natural frequency. The equation:

$$\frac{\Delta m}{A} = -\frac{\sqrt{\rho_q \mu_q} \Delta f}{2f_0^2} \quad (14)$$

where  $\rho_q$ ,  $\mu_q$  and  $A$  are the density, shear modulus and active area of the quartz crystal. Knowing the density of deposited material and time of deposition then gives the thickness of deposition as well as deposition rate.

## 1.10 Photocurrent Measurement

Typical photocurrent setup is not sufficient to measure BPVE as the expected current is in the order of magnitude of nA. This means that the current is easily overwhelmed by noise and is difficult to be picked up. Therefore, two key components are needed to measure the photocurrent, and they are the lock-in amplifier and optical chopper. The lock-in amplifier is an apparatus that helps separate an extremely weak signal from noise. It operates on the principle of homodyne detection. Meanwhile, the optical chopper is a disk with vanes patterned on it. Driven by an electric motor, a specific chopping frequency can be provided based on the respective rotation

frequency.

For a lock-in amplifier to function, it needs a reference signal with the same frequency as the signal that needs to be separated from the noise. Firstly, the lock-in amplifier removes the DC component of the signal, or the offset voltage. As any signal can be described as a combination of sine waves through Fourier series and since the time average of any combination of non-offset sine waves is zero, the signal then also has a time-average of zero after removing the offset voltage.

Next, the signal and reference are multiplied together. Segments of the signal that has matching frequencies with that of the reference then mixes and give rise to a new signal, in which it has a time-average value that can all be either positive, negative or zero, depending on the phase relation between the signal and reference. Therefore, the noise portion of the signal, that is not in frequency with the reference, will produce a signal known as a heterodyne signal, in which its time-average is zero. However, if the signal and reference are in frequency and have a constant phase relationship, then they will produce a signal known as a homodyne signal, in which its time-average value is non-zero. This suppresses the noise from the signal. This signal is then amplified and measured as needed.

The reference signal can therefore be provided by an optical chopper. By placing the optical chopper in the path of the laser, it can then modulate the laser based on the chopping frequency it was set to. The optical chopper can then be connected to the lock-in amplifier, therefore providing it with the reference signal while the chopped laser will be the signal that is needed to be locked on to.

## setup

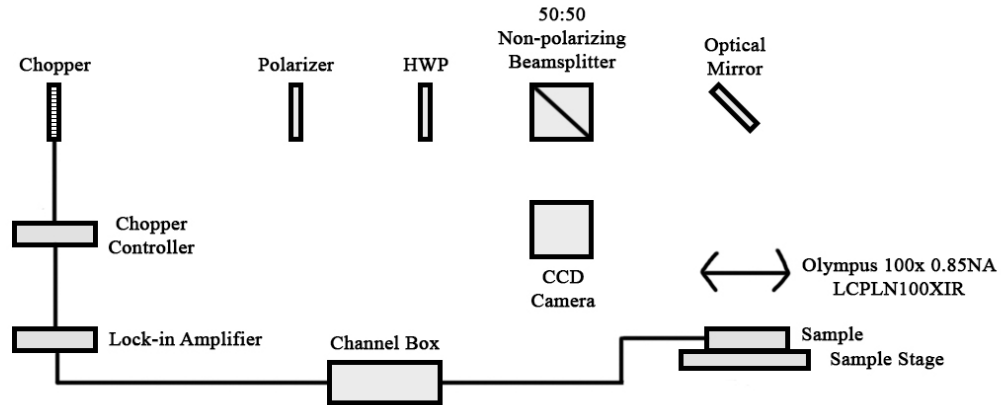


**Figure 6:** Schematic of the in-house setup used for photocurrent measurement. Solid lines represent wire connections

## 2 Methodology

### 2.1 Sample Fabrication

A 1cm by 1cm Silicon substrate is cut out from a Silicon wafer using a pen knife and then cleaned using a blower pump to remove any dust. It is then placed into a beaker of acetone acid that is enough to submerge the substrate. Acetone acid is used as it is effective in removing oil and organic residues that may be on the substrate surface. The substrate is then water bathed in a Grant Ultrasonic Waterbath for 3 minutes at room temperature. Next, the substrate is then submerged in a beaker of Isopropyl Alcohol (IPA) and water bathed again for 3 minutes. IPA is needed so as to remove any residual acetone acid that may remain on the surface. Afterwards, the substrate is then blow dried with N<sub>2</sub> gas as N<sub>2</sub> is an inert gas.

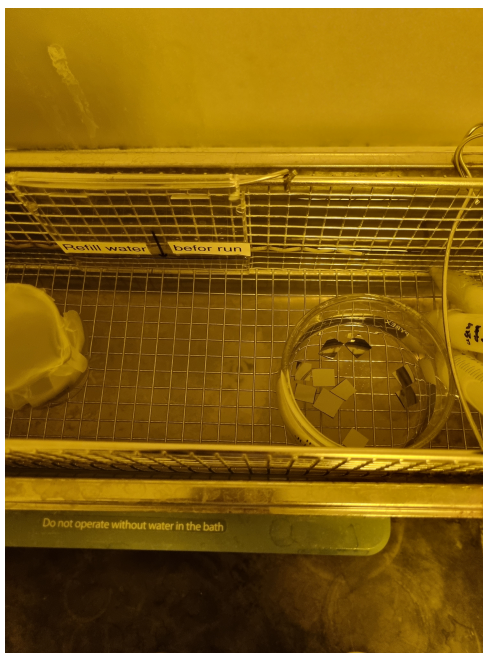


**Figure 7:** Samples being cleaned in a water bath.

Using a blue adhesive tape, flakes of PdSe<sub>2</sub> are exfoliated from the bulk sample and imparted onto the surface of the Silicon substrate. The sample is then observed under a microscope to locate a flake of suitable size, ideally about 10μm by 10μm and uniformed in thickness of less than 20nm, though getting such a flake is difficult due to the uncontrollable nature of mechanical exfoliation. Once a flake is found, their thickness is then determined through AFM using a Park Systems Atomic Force Microscope before SHG mapping is performed on it.

## 2.2 Atomic Force Microscopy Process

Firstly, the sample is loaded onto a metallic platform and afterwards placed onto the magnetic stage of the AFM. Alongside this, a non-contact cantilever is installed onto the head of the AFM by placing it onto its magnetic housing. The head is then slid into the machine through its grooves and the atomic force microscope is assembled.

Next, the laser is turned on by flicking a switch on the side of the machine and the tip of the cantilever is focused and centered on the camera. Similarly, the laser spot has to be centered at the cantilever's tip too. This can be achieved by rotating the pair of knobs on the AFM head. The laser spot is considered centralized when the software displays it as a green spot at the center of a grid. This laser spot has to also be in focus, which can be determined by ensuring that the software reads a voltage of about 2.7V from the cantilever and a Q-factor of 520Hz. When both these requirements are achieved, scanning of the sample can therefore begin.

The cantilever is slowly lowered to a height of  $9300\mu\text{m}$  and the camera focus is switched from the tip of the cantilever to the sample surface. Once the target flake has been located, the scanning area is then defined through the software as well as the resolution, which in this case, was 256 pixels. Then, the cantilever tip is ordered to automatically approach the flake slowly and the scanning begins. SHG mapping is then performed afterwards.

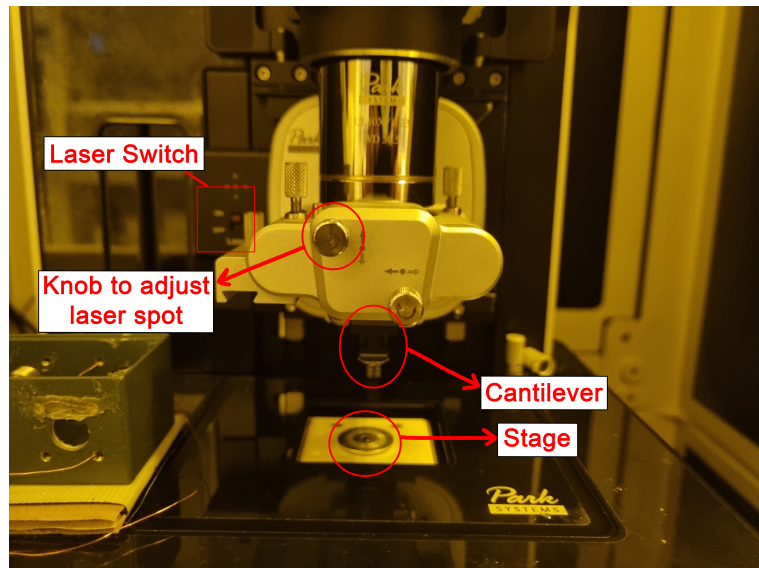


**Figure 8:** Park Systems AFM used to determine flake thickness.

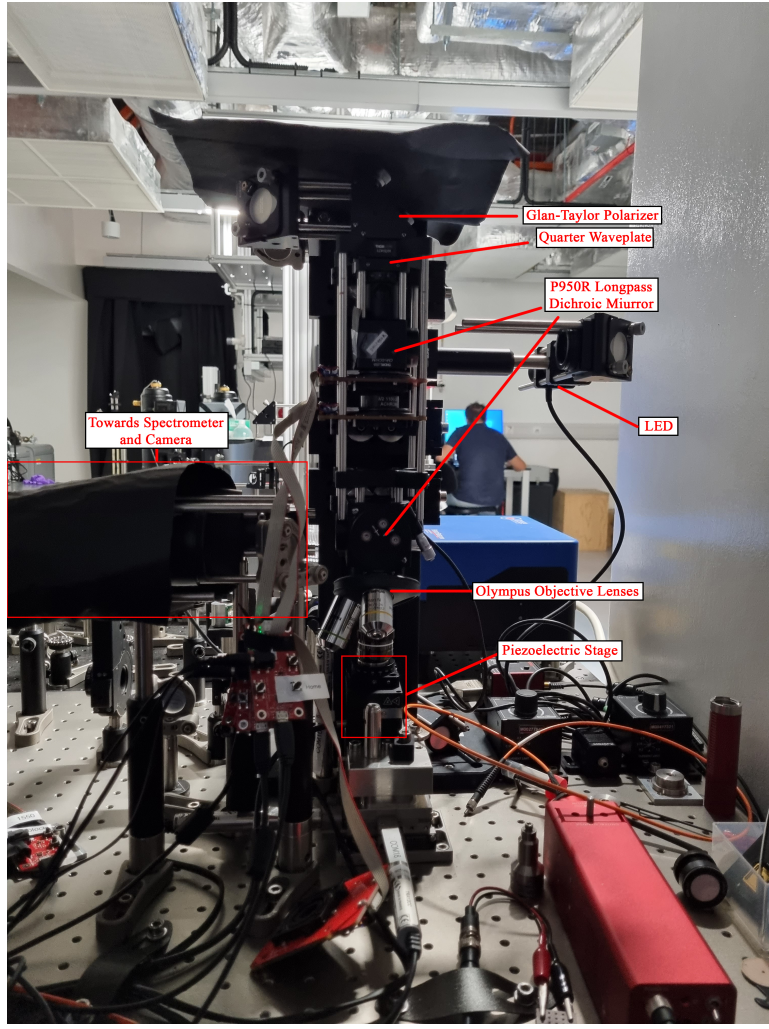


**Figure 9:** Labelled in-house setup used for SHG mapping.

### 2.3 Laser Lithography Process

Proceeding that, the sample is prepared for laser lithography. Using a dropper, three to four drops of LOR3A is dripped onto the sample such that the surface is sufficiently coated. The sample is then placed in a Polos spincoater and cycled at 7000 rotations per minute for 70 seconds. Then, it is baked at 175°C for 5 minutes. Afterwards, the sample is coated in three to four drops of S1805 and cycled also at 7000 rotations per minute for 70 seconds. Lastly, the sample is then baked at 135°C for 5 minutes.

The sample then undergoes laser lithography with the respective electrode designs that can be found in *Appendix 1*. Lastly, it is submerged in a beaker of MF319 for 50 seconds before being washed with distilled water and dried with N<sub>2</sub> gas. After laser writing, the sample is examined

a microscope to ensure that the design has been drawn properly.

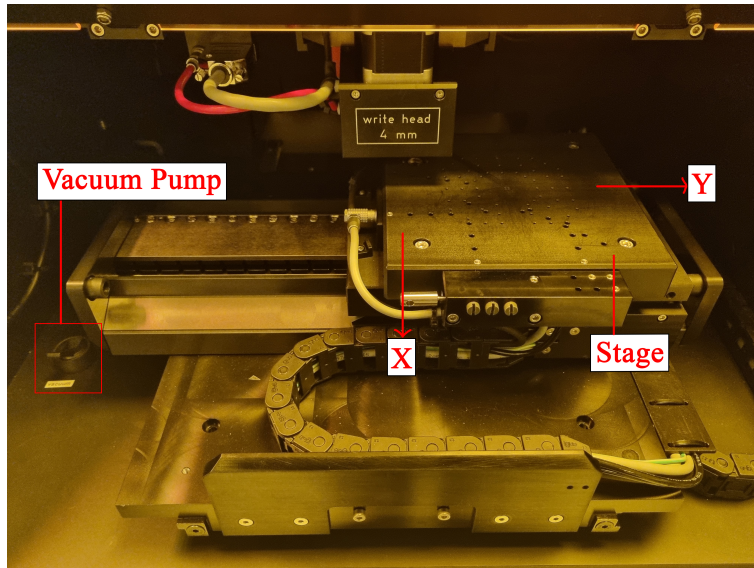


**Figure 10:** Laser writer in which the sample undergoes laser lithography. The sample is fixed in placed at the center of the stage by the vacuum pump and has to be oriented based on the stage's orientation.

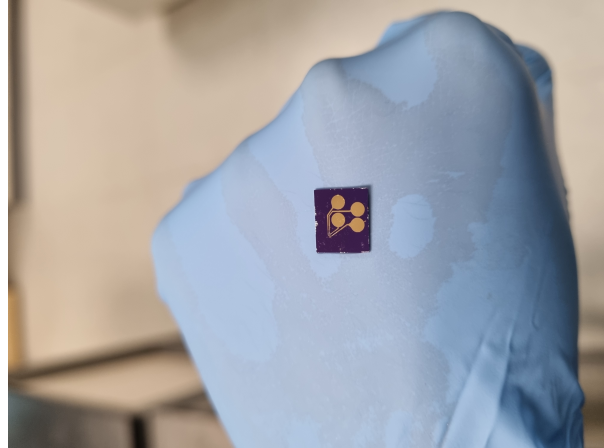
## 2.4 Vapor Deposition Process

Vapor deposition is then performed in the *Angstrom* Vapor Deposition machine. The sample is first affixed onto a crucible with high-heat resistant *Kapton* tape around the perimeter of the sample such that it does not block the electrode pattern to be filled. It is then placed into the deposition chamber where the shutters are closed and the chamber is then evacuated to  $10^{-7}$  Torr. Once so, deposition process then begins.

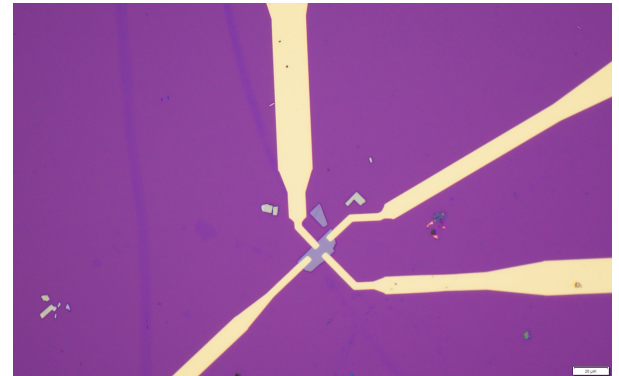
Chromium and Gold will be used in the deposition process. Chromium is firstly deposited as it acts as a form of adhesive between the sample surface and Gold. For optimum adhesion, Gold needs to form oxide bonds with the substrate, but being a noble gas, it is difficult for it to do so. However, Chromium readily bonds with the Silicon substrate or any silicon oxide layer on its surface. Therefore, when Gold is then deposited on this Chromium intermediary layer and the sample is then heated, a Chromium-Gold alloy will form, allowing the gold to remain on the sample.

As power through the Chromium crucible is generally increased, the rate of evaporation of Chromium increases too. When it reaches a stable value, the thickness value of the sample

is set to zero and the shutters are opened. Chromium is then deposited onto the sample until a thickness of 3nm has been reached. A similar process is repeated for Gold such that 50nm of Gold has been deposited on the sample. Lastly, the sample is then submerged in a beaker of PG Remover. It is then heated at 60°C for one hour.



(a)



(b)

**Figure 11:** (a) Image of a finished sample with gold electrodes. (b) Microscopic view showing the contact between electrode and flake.

## 2.5 I/V Sweep

The I/V Sweep is performed on a probe station. The sample is loaded onto the stage and two probe tips are then moved into contact with a pair of electrode pads through pairs of knobs located at the base of the probe that either shift the probe tip horizontally or vertically. A voltage range of  $-3V$  to  $3V$  was applied across the sample and the corresponding current obtained was then measured.

## 2.6 Photocurrent measurement

The optical chopper is placed in the path of the laser and connected to the *Stanford Research System SR830* digital lock-in amplifier. A chopping frequency of 499Hz was set. The sample is fixed onto the stage by using double-sided tape. Optical mirrors within the setup can be adjusted to align the laser onto the central part of the sample. The laser is considered aligned when defocusing the laser does not shift it from its initial location. Lastly, a channel box is connected to the lock-in amplifier. This channel box is also connected to the sample's electrode pads and when performing measurements across a pair of electrodes, one of them will be grounded. Neutral density filters

are filters that reduces the intensity of all wavelength across the spectrum equally. By applying neutral density filters ranging from ND0.5 to ND3, where ND 1 is 10%, ND2 is 1% and so on, the power of light being transmitted can be controlled and the power dependence relation of the shift current can therefore be determined accurately.

### 3 Results & Discussion

#### 3.1 Flakes from mechanical exfoliation

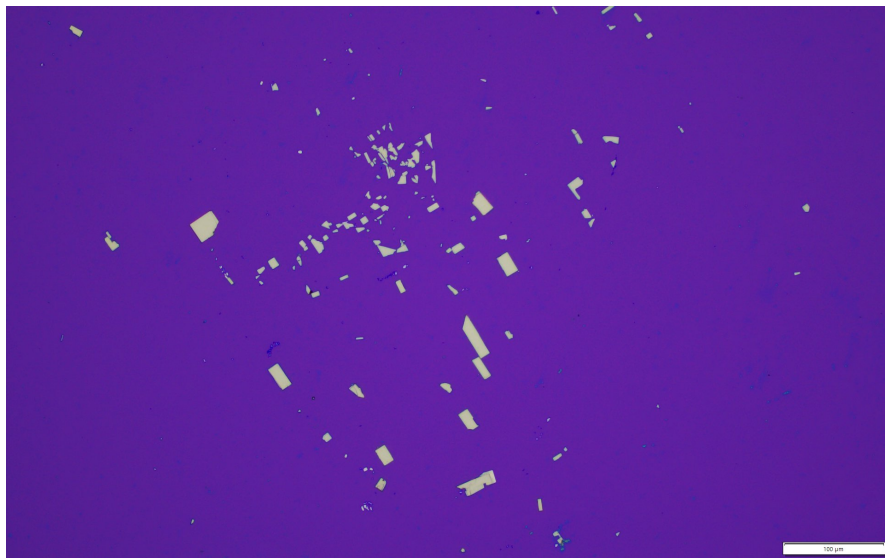


**Figure 12:** Flakes of PdSe<sub>2</sub> captured under  $\times 20$  magnification.

PdSe<sub>2</sub> flakes obtained from mechanical exfoliation of the bulk sample were mostly larger than the target  $10\mu\text{m}$  by  $10\mu\text{m}$  area size. However, the issue comes with their thickness, which generally gave a measured value of about 36 monolayers and above. This makes such flakes unsuitable for device fabrication as their properties may deviate even further from the 2D properties that is being measured. One such property is the bandgap of PdSe<sub>2</sub>, which decreases from 1.6eV to 0eV as it approaches the bulk. As can be seen from **Fig.13** below, majority of the flakes are thick considering that they have a white-blue color to them. Flakes that are sufficiently thin would take on the purple hue of the Silicon substrate.

Another potential issue is that the flakes are not of uniformed thickness, which means that deviations in the photocurrent measurement may also be dependant on the location on the flake that is being measured.

Flakes that were of about 20 monolayers and lower were mainly shattered and too small to be used for device fabrication. Throughout the project, four flakes of appropriate size and thickness were obtained, but only two were used.

### 3.2 Atomic Force Microscopy Measurement

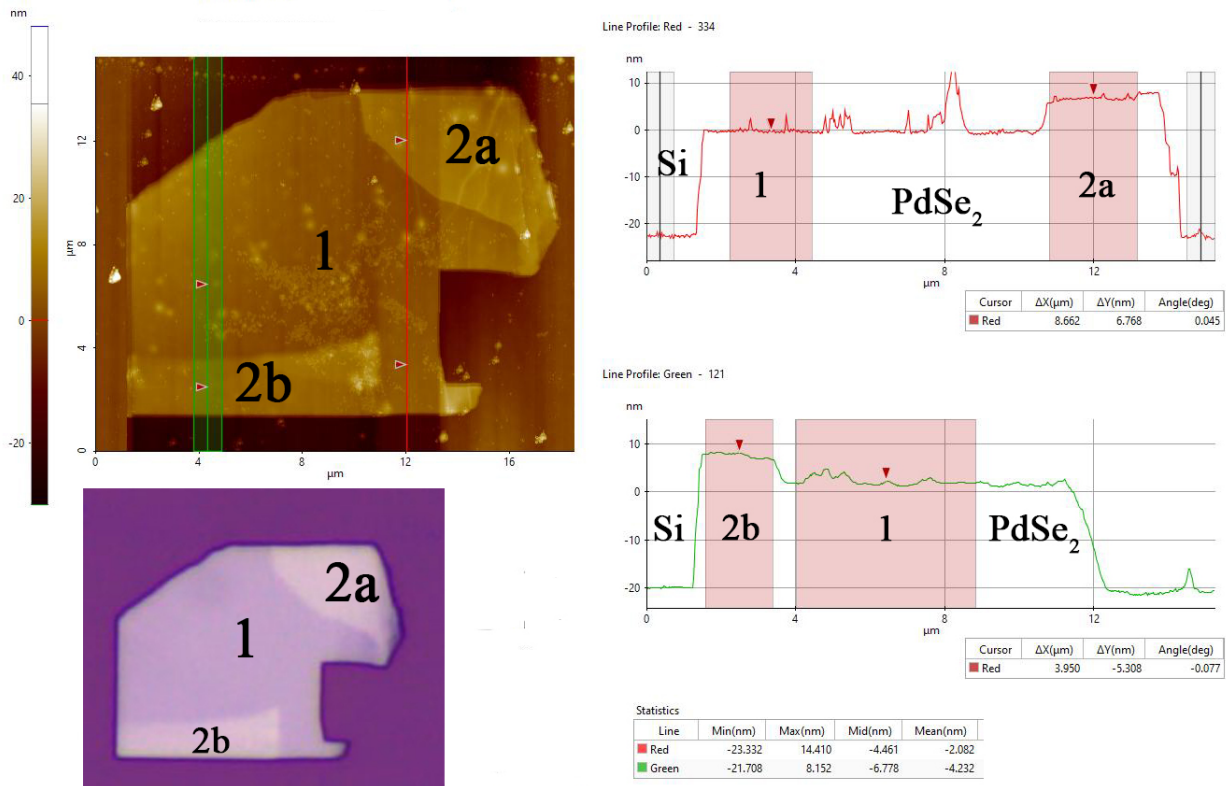


**Figure 13:** AFM measurement of Flake 1.

Flake 1 was measured to be approximately  $15\mu\text{m}$  by  $15\mu\text{m}$  using the in-built microscope measuring tool. The red graph beside the AFM image denotes the corresponding thickness measured across a particular axis, which is demarcated by the red line on the AFM image. Meanwhile, the green graph shows the thickness obtained across the green line when it is averaged over a small region. This region is displayed as the translucent green areas beside the green line. The red arrows denote the corresponding thickness for a particular point on the flake.

As can be seen from the AFM image of Flake 1, there appears to be two major regions of different thickness within Flake 1; Region 1 is colored purple while the other, Region 2a and 2b, has a lighter pink tinge to it. This is further supported by the thickness shown in the red graph. As the measurement crosses the boundary between the two regions, there is an abrupt change in thickness of 6.768nm between Region 1 and 2a and 5.308nm between Region 1 and 2b. These give a difference of about 9 monolayers and 7 monolayers respectively. Therefore, there has to

be a change from either odd to even layers or vice versa whenever these boundaries are crossed due to the odd-layer difference between them.

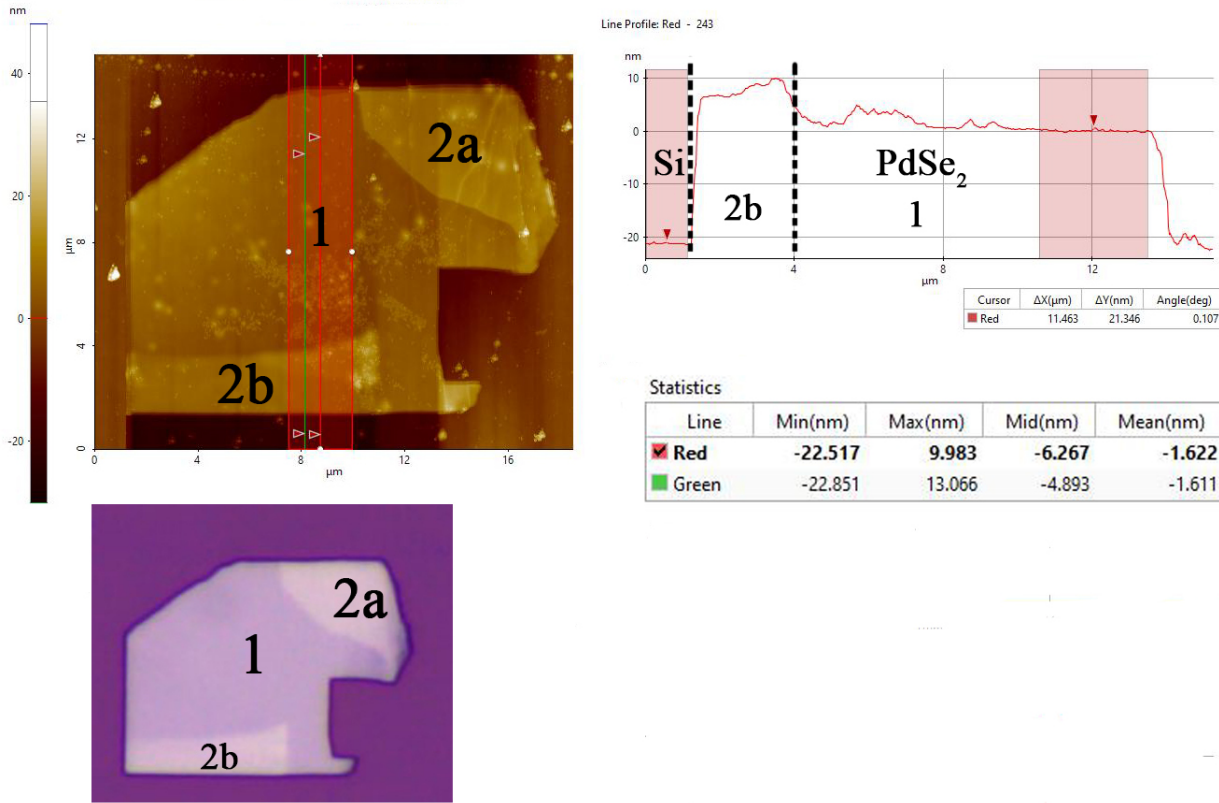


**Figure 14:** Thickness of Flake 1.

The measured thickness for Region 1 of Flake 1 was measured to be 21.346nm, which gives 28 monolayers. As such, it is expected for Region 1 to show SHG response as it is even-layered and its structure have a broken centrosymmetry. Similarly, Region 2a and 2b have to be odd-layered due to the odd-layer difference as compared to Region 1. Region 2a and 2b are expected then to not show any SHG response as they have centrosymmetry.

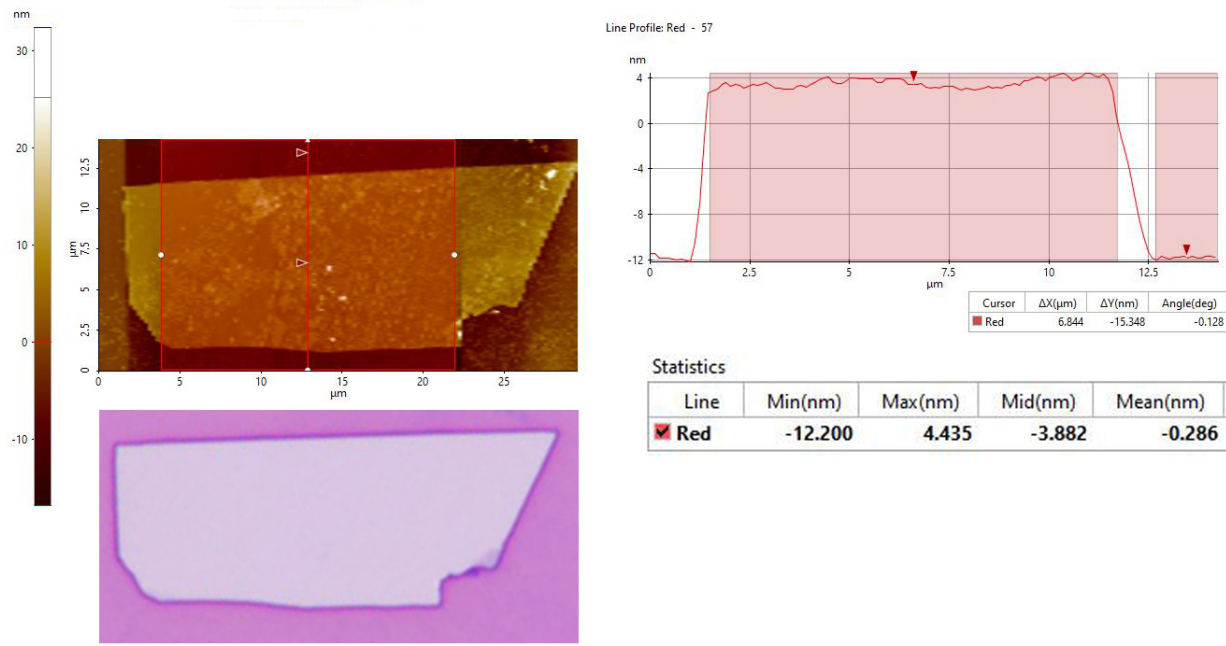


**Figure 15:** AFM of Flake 2.

Meanwhile, Flake 2 is approximately  $10\mu\text{m}$  by  $23\mu\text{m}$  with an average thickness of 15.348nm, which gives about 20 monolayers. Its uniformly even-layered thickness makes it an ideal candidate for photocurrent measurement as the shift current would not be influenced by a competing drift current from centrosymmetric regions<sup>8</sup>. Centrosymmetric regions produce this competing drift current as they are influenced by the internal electric field due to the polarization of non-centrosymmetric regions in the presence of an external electric field, like light.

### 3.3 SHG Mapping

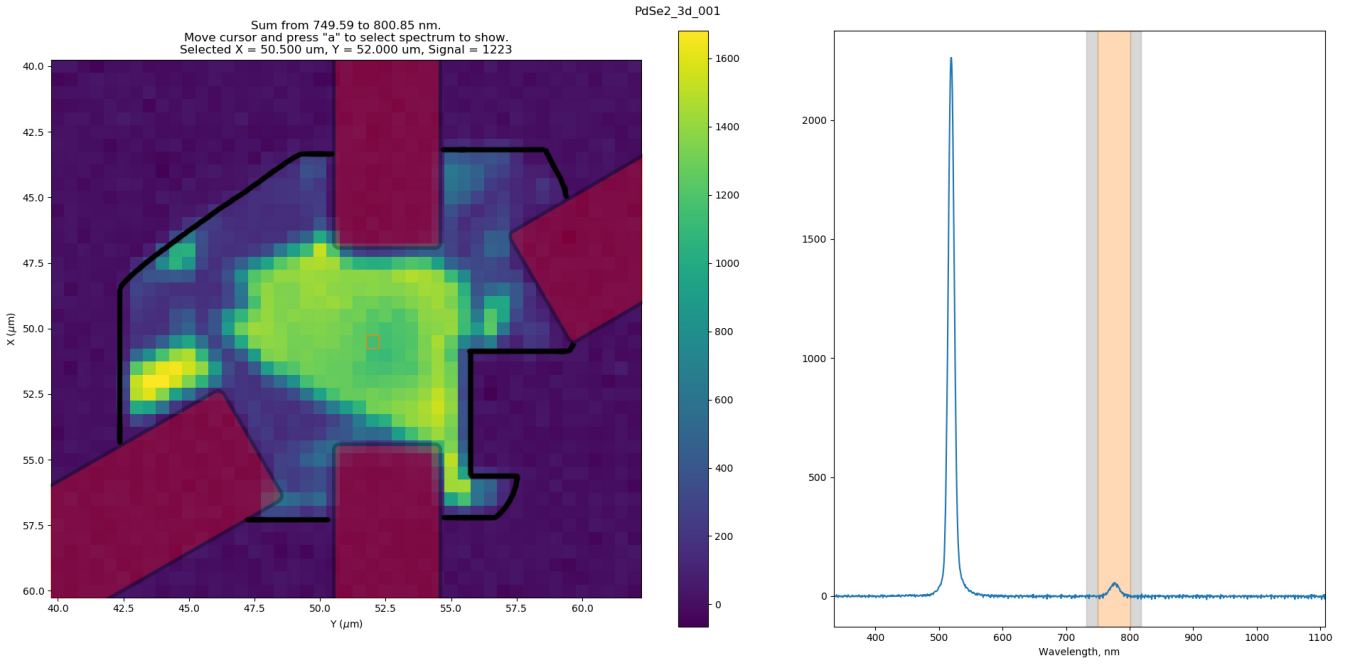


**Figure 16:** SHG Mapping of Flake 1.

Flake 1 demonstrated strong SHG response when it underwent SHG mapping using 1550nm laser. The SHG mapping on the left of **Fig.16** consists of two particular regions of interest, the areas that are in dark blue, and the others colored in green. Each pixel is an intensity value that is obtained by integrating the intensity response received across the wavelength after frequency doublings. Since the wavelength of laser used was 1550nm, this integration range should be around the 775nm region. This is shown on the graph on the right side of **Fig.16**. The regions of green correlates to areas that produced a high intensity SHG response. The other high intensity response around 515nm corresponds to the third-harmonic generation (THG) process. It can be seen that Region 1, as mentioned in Section 4.3 displayed strong SHG response due to it being even-layered and having broken centrosymmetry structure while those of Region 2a and 2b did not display SHG response as they were of odd-layers and therefore, had centrosymmetry.

However, within Region 1 there were some areas that did not display SHG, specifically the top-left corner. As our sample was exposed to atmospheric conditions over a period of several months, it is possible that a layer of  $\text{PdO}_2$  was formed on the surface<sup>9</sup>. As  $\text{PdO}_2$  belongs to the space group 136, which is centrosymmetric, and since the SHG mapping is a surface probing method, there would not be any SHG response in that area, therefore leading to a smaller than

expected SHG response area within Region 1.

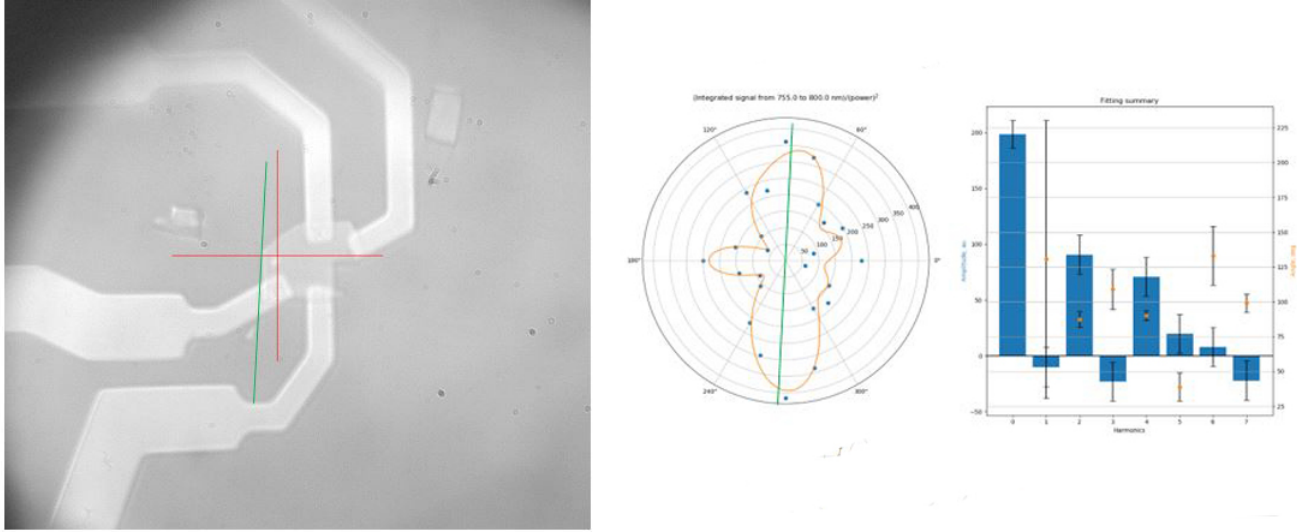


**Figure 17:** Angle-dependant polarization spectroscopy of Flake 1.

Aside from the intensity of the SHG response, the SHG mapping also allows the determination of the crystallography axis of the flake. The left side of **Fig.18** is the optical image of the flake with the direction of strongest polarization, marked in green, drawn upon it. The graph on the right hand side represents the various amplitudes of arbitrary units when fitted to the various harmonic generation process. The zero order harmonic generation, in an ideal fitting, is the sum of all the other ordered harmonic generation process.

Referencing other literature<sup>10</sup>, the a-axis of the PdSe<sub>2</sub> crystal structure, labelled in **Fig:1**, corresponds to the degree of largest polarization in the angle-resolved polarization spectroscopy shown in **Fig:18**. The shift current is therefore expected to flow in the direction of largest polarization<sup>11</sup>. This is because the larger the degree of polarization, the greater the asymmetrical interference between the excitation amplitude of the electrons and this produces a greater shift current.

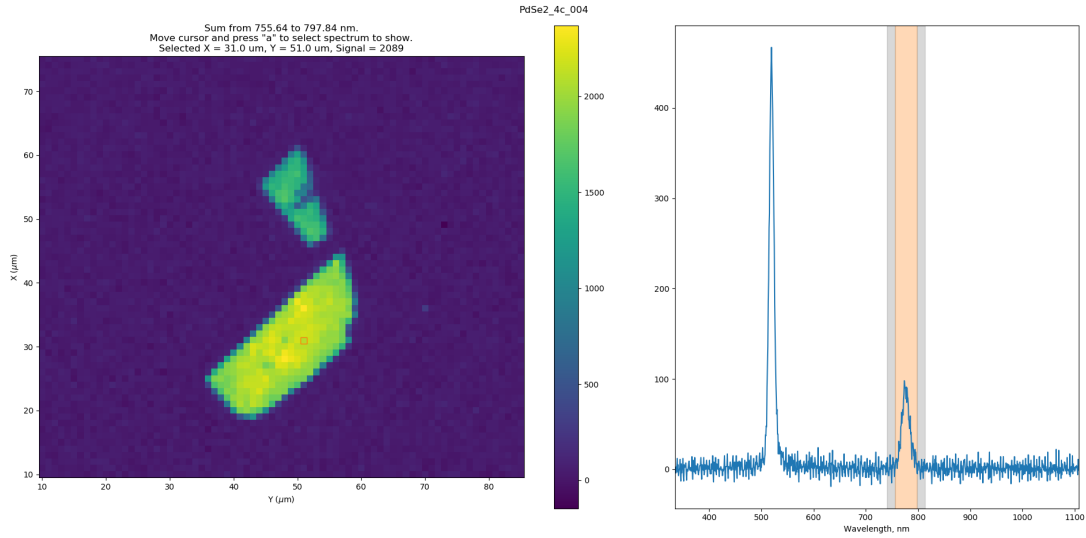


**Figure 18:** SHG mapping of Flake 2

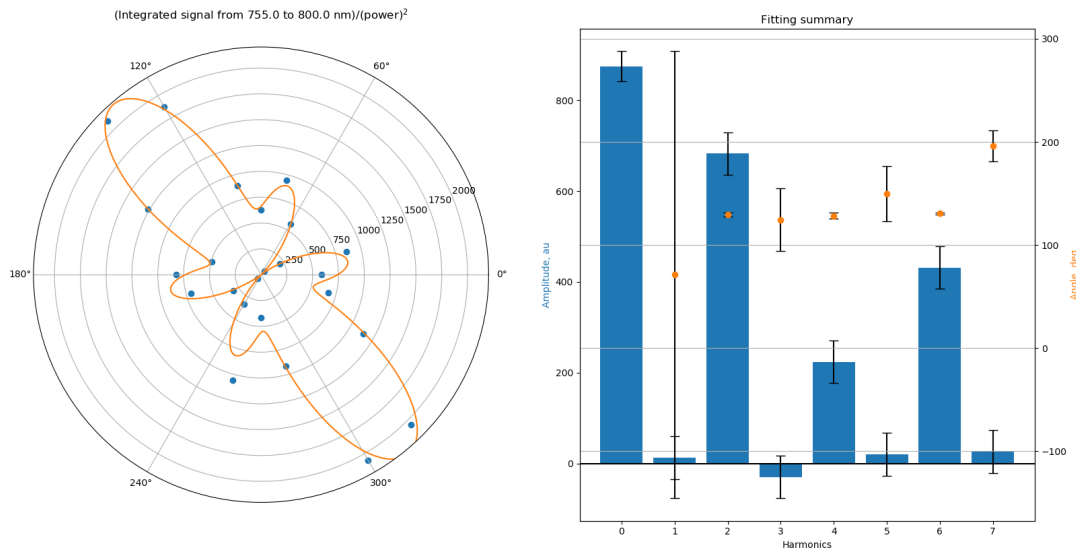


**Figure 19:** Angle-dependent polarization spectroscopy of Flake 2

The SHG mapping of Flake 2 shows a nearly uniform SHG response across the surface of the flake. This further affirms the uniform even-layered thickness throughout Flake 2. Additionally, a similar 2-petal pattern for the polarization spectroscopy of Flake 2 was also obtained. It can be seen that the intensity response of the SHG signal for Flake 2 is much stronger than that obtained from Flake 1. Flake 2 has an intensity value of about 680 while Flake 1 had less than 100. Flake 2 has a larger SHG response due to it being a thinner flake. This is because as the flake thickens and resembles more of the bulk, its space group shifts from the non-centrosymmetric

Pca<sub>2</sub><sub>1</sub> to the centrosymmetric Pbca<sup>12</sup>. Therefore, the asymmetrical interference of the excitation amplitude becomes lesser and this gives the lesser SHG response in thicker samples.

### 3.4 I/V Sweep

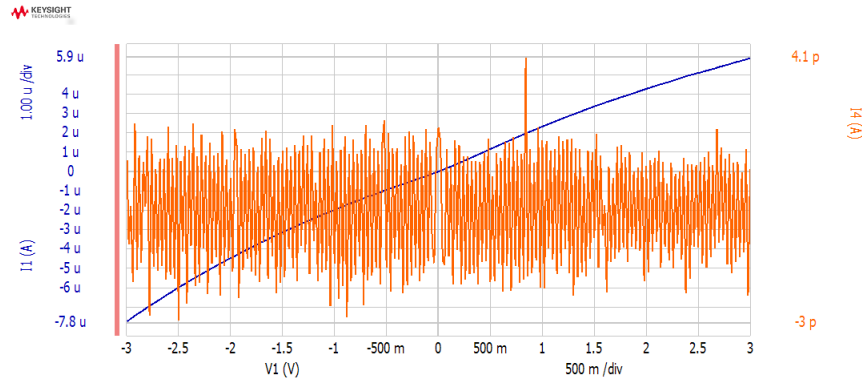


**Figure 20:** I/V sweep of Flake 1 from -3V to 3V. Blue graph represents the current flowing through the device while the orange graph is for errors in the reading.

An I/V sweep was performed on Flake 1 to determine condition of the electrode contacts with the sample. It can be seen that the orange sweep is in order of magnitude of picoampere. Compared to the current which is of microampere, the error is therefore negligible and this means that the Gold electrodes are in good contact with Flake 1.

### 3.5 Photocurrent Measurement

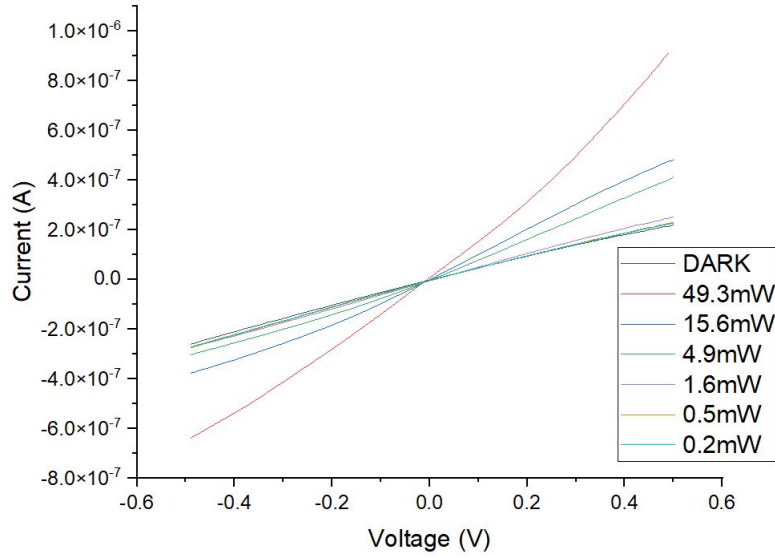


**Figure 21:** I/V sweep of Flake 2 for Channel 1,4 (where 4 is grounded) illuminated under 473nm wavelength of maximum power 156mW.

As the intensity of light was increased from 0.2mW to 49.3mW, we can see a corresponding increase in the gradient of the I/V curve respectively. This is because as the intensity of light increases, we expect there to be more available photons to excite the electrons to produce the expected photocurrent. Therefore, the magnitude of the current at 0V has to increase too and this gives rise to the steeper gradient of the I/V curve.

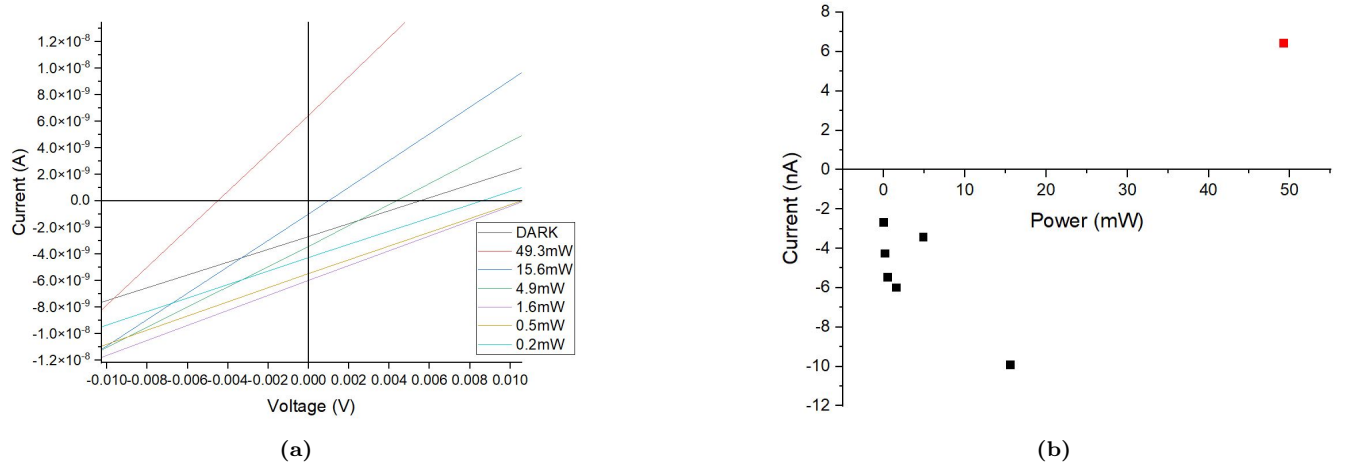


**Figure 22:** (a) Zoomed in graph of Fig.21 around the origin. (b) Short circuit current of Flake 2 for Channel 1, 4 under 473nm light.

In fact, if the photocurrent value at short circuit (0V) was plotted, the graph appears to be approaching a saturation level. However, this behavior could not be confirmed as the current switches direction immediately after. This switching of current at 49.3mW could be due to the onset of conventional current produced from thermal excitation dominating the system. Additionally, the full power of the laser, at 156mW, was not used in the measurement as PdSe<sub>2</sub> was theorized to have a Seebeck coefficient of  $300\mu\text{V/K}$ <sup>13</sup>. There was a risk that the laser could burn and damage the sample.

### 3.6 Photocurrent Mapping

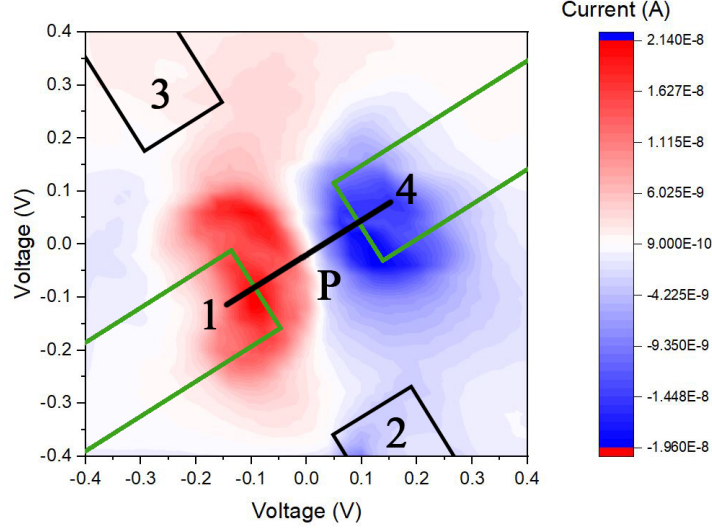


**Figure 23:** Photocurrent Mapping of Flake 2 for Channel 1,4 from -0.4V to 0.4V using 473nm light, where P denotes the polarization axis obtained from SHG mapping.

The photocurrent mapping obtained for Flake 2 shows that photocurrent response was mainly near the active electrodes of 1 and 4. Other than those regions, photocurrent was almost absent. This photocurrent profile closely depicts that of a Schottky barrier photocurrent rather than the shift current. If it was the latter, the entire sample would show photocurrent with a clear divide between two regions of positive and negative photocurrent around the active electrodes.

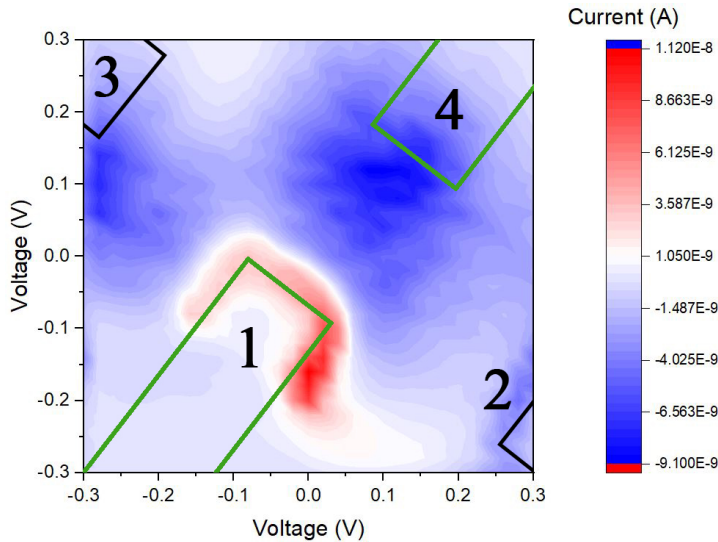


**Figure 24:** Photocurrent Mapping of Flake 2 for Channel 1,4 from -0.3V to 0.3V using 473nm light.

A mapping possibly resembling shift current was obtained when a repeated measurement

was performed on a different day. There is a clear shift current throughout the entire sample flowing from electrode 4 to electrode 1. Regions further away from these two pair of electrodes produces a weaker shift current, except for the area in the top left near electrode 3. A similar peculiarity is noted in **Fig.23** at the left side near electrode 3, albeit much weaker. One probable explanation is that the local asymmetry was enhanced due to stress induced by the nearby electrode<sup>14</sup>, therefore allowing that particular region to produce a larger shift current.

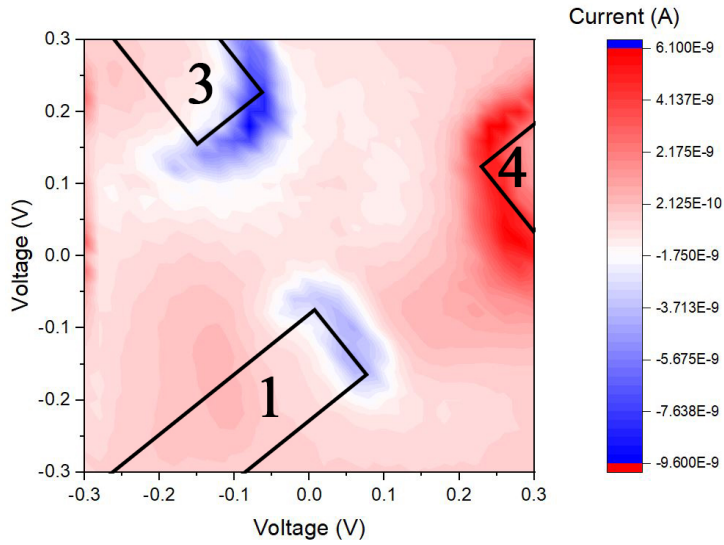


**Figure 25:** Photocurrent Mapping of Flake 2 for Channel 3,2 from -0.4V to 0.4V using 473nm light.

Electrode 3 and 2 were then measured to compare against. As they are not in the direction of polarization, a shift current is not expected. Similarly, a strong Schottky effect was observed around the electrodes 3, 1 and 4, despite 1 and 4 being grounded for the measurement. There also appears to be an weak ambient current throughout the sample. Despite so, even if the measurement was zeroed to this ambient current, the Schottky barrier effect would still persist around the electrodes. One possible explanation for this observation is that the sample has heated up and conventional current is present within. Each mapping took a duration longer than an hour and no Neutral Density filter was applied to the laser. This would explain the heat up of the sample constant ambient current throughout. Moreover, as the electrons in the sample are thermally excited, those near the electrodes would have enough energy to bypass the Schottky barrier. Therefore, a short circuit might have occurred between electrode 3 and 4 as well as 3 and 1 and this may explain the unexpected Schottky barrier around the unused electrodes.

## 4 Conclusion

### 4.1 Summary

In conclusion, samples of PdSe<sub>2</sub> were fabricated on Si wafer and Gold was used to form the electrodes. Data from the SHG mapping performed was able to verify the theory that there was a need of inversion breaking within the crystal structure for there to have a SHG response. However, the shift current was unable to be verified due to the strength of the Schottky barrier. From the SHG mapping, it can be seen that the possible shift current observed in **Fig.24** was of the magnitude  $10^{-9}\text{A}$ , whereas the Schottky was able to reach  $10^{-8}\text{A}$  in **Fig.23**. Due to the high Seebeck value of PdSe<sub>2</sub> ( $300/K$ ), temperature was an additional factor that should have been considered when conducting the photocurrent measurement. While the aim was to verify the shift current within PdSe<sub>2</sub>, the effect of temperature on the BPVE is a potentially interesting field that could be investigated further on.

### 4.2 Follow-up to Experiments

Much time was used in obtaining a sample of suitable size and thickness for the photocurrent measurement. Gold-assisted exfoliation could be a more efficient method to obtain flakes with extremely thin layers but of large areas<sup>15</sup>. Additionally, due to its high Seebeck value, a study into the relationship between the temperature of the flake and the photocurrent could also be performed. This could be done by placing the device in a temperature chamber and performing the photocurrent mapping from near 10K to 300K. Lastly, another study that could be done is to measure the photocurrent with respect to the polarization of the light. Theory suggests that the the magnitude of the photocurrent should behave sinusidually with the polarization angle. While an attempt was made in this project, there was no observable change in value of the photocurrent, and therefore, not reported.

### 4.3 Future Research

Most currently available material regarding PdSe<sub>2</sub>, as of this thesis. are theoretical. This means many potential experiments to verify the theories proposed. One potential avenue for study is the effect of strain on the photocurrent. As it is possible for strain to improve the photovoltaic capabilities in other TMDCs semiconductor, PdSe<sub>2</sub> would therefore also be a great candidate to observe if such effect occurs for it too. Not only that, but the charge moblity and Seebeck

coefficient could also be verified. Lastly, further attempts to find shift current in PdSe<sub>2</sub> could also be performed. Despite numerous paper theorizing its high shift current, there is yet to be any experimental confirmation on it.

## 5 Appendix

### 5.1 Electrode Design

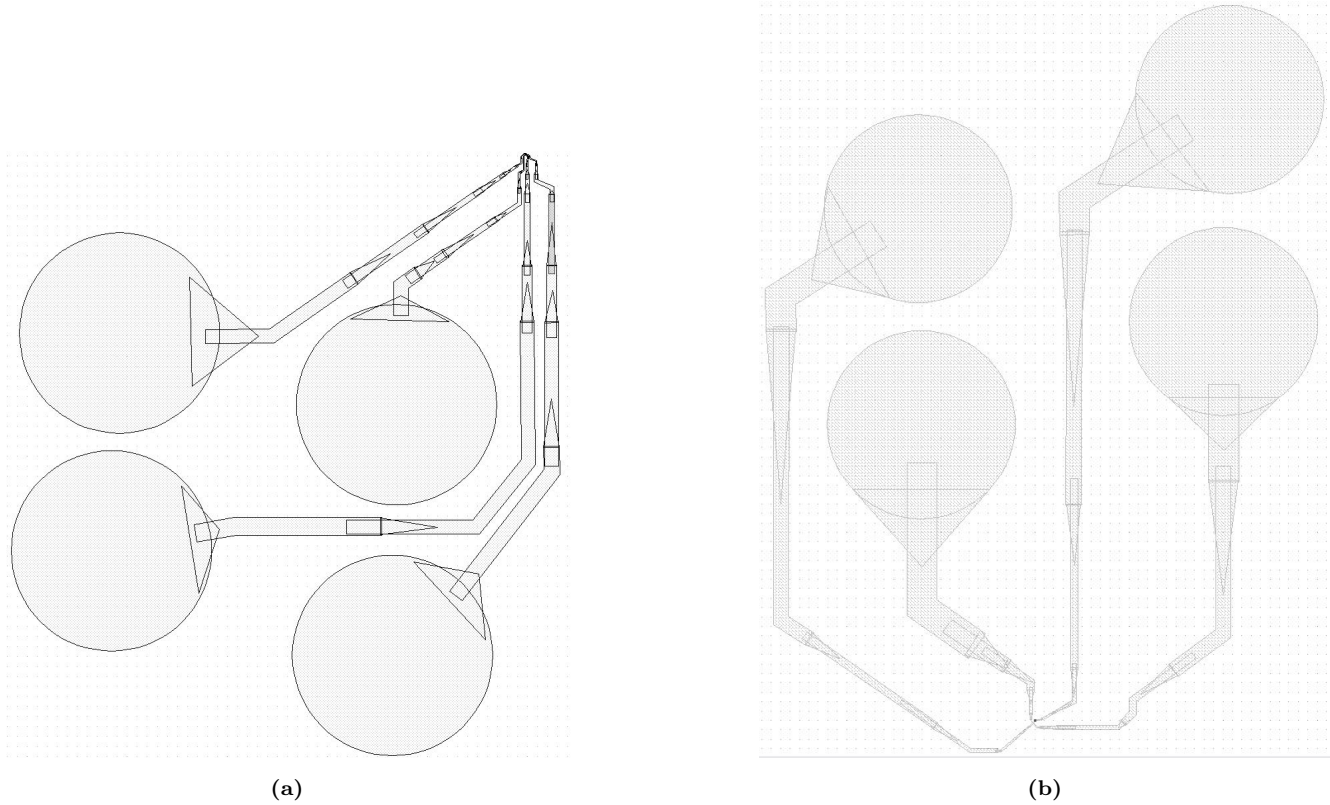


**Figure 26:** (a) Electrode design of Flake 1 (b) Electrode design of Flake 2. Each designs were aligned to the direction of largest polarization obtained from SHG mapping.

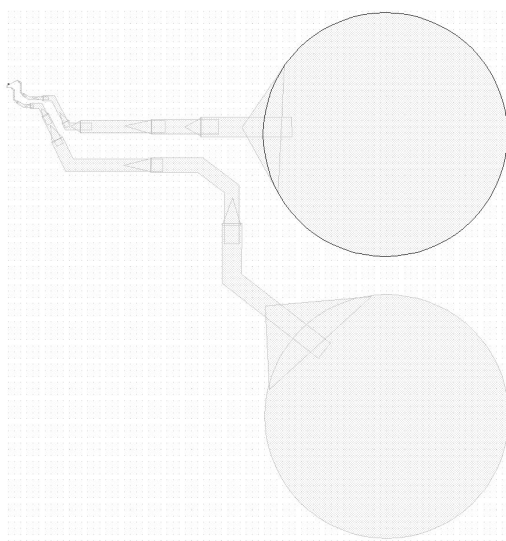


**Figure 27:** Electrode design for the unused Flake 3.

## 5.2 Unused Samples

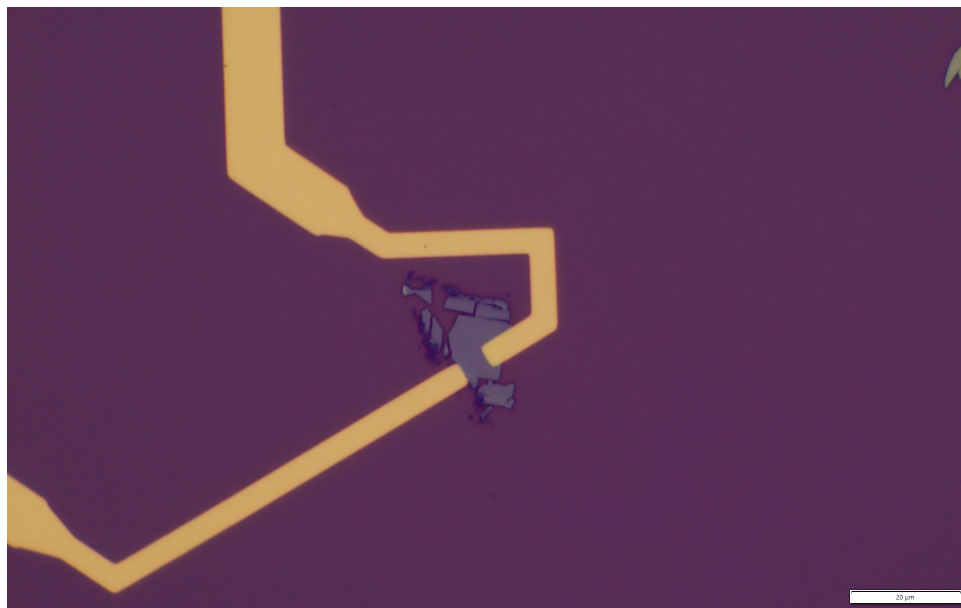


**Figure 28:** During the laser lithography phase for Flake 3, the electrodes were not properly aligned to the zero coordinate on the sample. This resulted in the electrodes being shifted partially and minimal contact with the flake for the bottom electrode.

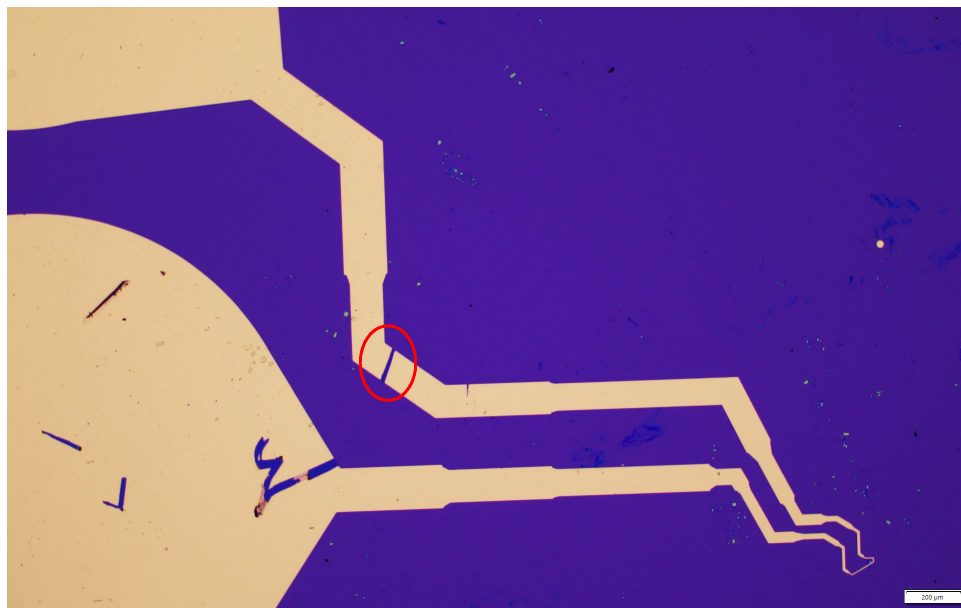


**Figure 29:** One of the Gold electrodes was scratched off Flake 3, possible due to mishandling of the sample with a tweezer. One solution was to apply silver paste to the affected area to reconnect the electrode.



**Figure 30:** x100 microscopic image of Flake 4. Measuring  $32.19\mu\text{m}$  by  $37.82\mu\text{m}$  it was unused due to its irregular shape and various regions in thickness visible from the different shades of purple.

## 6 References

1. Rubén Mas-Ballesté, Cristina Gómez-Navarro, Julio Gómez-Herrero, Félix Zamora. (2011). "*2D materials: to graphene and beyond.*" *Nanoscale* (3). p.20-30.  
<https://doi.org/10.1039/C0NR00323A>
2. He Tian, Jesse Tice, Ruixiang Fei, Vy Tran, Xiaodong Yan, Li Yang, Han Wang. (2016). "*Low-Symmetry Two-Dimensional Materials for Electronic and Photonic Applications.*" *Nano Today*. p.1, 2, 26.  
<https://doi.org/10.1016/j.nanotod.2016.10.003>
3. Yanhao Wang, Jinbo Pang, Qilin Cheng, Lin Han, Yufen Li, Xue Meng, Bergoi Ibarlucea, Hongbin Zhao, Feng Yang, Haiyun Liu, Hong Liu, Weijia Zhou, Xiao Wang, MarkH., Yu Zhang, Giancarlo Cuniberti. (2021). "*Applications of 2D-Layered Palladium Diselenide and Its van der Waals Heterostructures in Electronics and Optoelectronics.*" *Nano-Micro Letters* (13). p.3, 6, 5  
<https://doi.org/10.1007/s40820-021-00660-0>
4. Sean Raglow. "*Introduction to the Shift Current Photovoltaic Effect.*" p. 1
5. Hongbo Hu, Kai Wang, Hua Long, Weiwei Liu, Bing Wang, Peixiang Lu. (2015). "*Precise Determination of the Crystallographic Orientations in Single ZnS Nanowires by Second Harmonic Generation Microscopy.*" *Nano Letters* (15,5). p.3351-3357.  
<https://doi.org/10.1021/acs.nanolett.5b00607>
6. Robert W. Boyd. (2008) "*Non-Linear Optics*". p.38-40
7. Juan Yu, Xiaofei Kuang, Junzi Li, Jiahong Zhong, Cheng Zeng, Lingkai Cao, Zongwen Liu, Zhouxiaosong Zeng, Ziyu Luo, Tingchao He, Anlian Pan, Yanping Liu. (2021). "*Giant nonlinear optical activity in two-dimensional palladium diselenide.*" *Nature Communications* 12, 1083.  
<https://doi.org/10.1038/s41467-021-21267-4>

8. Chi-Kuang Sun.(2007) "Second Harmonic Generation Microscopy Versus Third Harmonic Generation Microscopy in Biological Tissues. In: Optical Imaging and Microscopy." Optical Sciences, vol 87. Springer, Berlin, Heidelberg. [https://doi.org/10.1007/978-3-540-69565-3\\_11](https://doi.org/10.1007/978-3-540-69565-3_11)
9. Anna N. Hoffman, Yiyi Gu, Liangbo Liang, Jason D. Fowlkes, Kai Xiao, Philip D. Rack. (2019). "Exploring the air stability of PdSe<sub>2</sub> via electrical transport measurements and defect calculations." 2D Materials and Applications (3), 50.
10. Wataru Nishiyama, T. Nishimura, Keiji Ueno, Takashi Taniguchi. (2022). "Quantitative Determination of Contradictory Bandgap Values of Bulk PdSe<sub>2</sub> from Electrical Transport Properties." Advanced Functional Materials 32(9):2108061. DOI:10.1002/adfm.202108061
11. Liang Z. Tan, Fan Zheng, Steve M. Young, Fenggong Wang, Shi Liu, Andrew M. Rappe. (2016) "Shift current bulk photovoltaic effect in polar materials-hybrid and oxide perovskites and beyond."
12. Vijay Kumar Gudelli, Guang-Yu Guo. (2021). "Large bulk photovoltaic effect and second-harmonic generation in few-layer pentagonal semiconductors PdS<sub>2</sub> and PdSe<sub>2</sub>." New Journal of Physics (23). p.2
13. Dan Qin, Peng Yan, Guangqian Ding, Xujin Ge, Hongyue Song, Guoying Gao. (2018) "Monolayer PdSe<sub>2</sub>: A promising two-dimensional thermoelectric material." p.4  
DOI:10.1038/s41598-018-20918-9
14. G. Abadias, E. Chason, J. Keckes, M. Sebastiani, G.B. Thompson, E. Barthel, G.L. Doll7, C.E. Murray, C.H. Stoessel, L. Martinu. (2018). "Stress in thin films and coatings: Current status, challenges, and prospects." Journal of Vacuum Science Technology A 36, 020801.  
<https://doi.org/10.1116/1.5011790>

15. Matej Velicky, Gavin E. Donnell, William R. Hendren, Stephen McFarland, Declan Scullion, William J. I. DeBenedetti, Gabriela Calinao Correa, Yimo Han, Andrew J. Wain, Melissa A. Hines, David A. Muller, Kostya S. Novoselov, Hector D. Abruna, Robert M. Bowman, Elton J. G. Santos, Fumin Huang. (2018) *"Mechanism of Gold-Assisted Exfoliation of Centimeter-Sized Transition-Metal Dichalcogenide Monolayers."* ACS Nano 12, 10463-10473